

Two-body transient viscous interactions in free space

Bo Liu  and Sukalyan Bhattacharya

Department of Mechanical Engineering, Texas Tech University, Lubbock, Texas 79409, USA



(Received 3 June 2021; accepted 17 September 2021; published 19 October 2021)

This article elucidates how unsteady hydrodynamic interactions between two closely situated spheres in a viscous liquid affect their time-dependent motion. The system represents typical Brownian particles for which temporal inertia is always comparable to the viscous forces even though convective inertia is negligible. The analysis quantifies the transient mutual interactions in terms of frequency-dependent friction coefficients of both spheres as well as their temporally varying mobility response to an impulsive force. To this end, a generalization of Stokesian dynamics is formulated, where instead of Stokes equation, linearized unsteady Navier-Stokes is Fourier transformed in frequency space to describe flow fields. Accordingly, two complete sets of basis functions for the Brinkman equation instead of the Stokes equation are constructed in spherical coordinates centered around two particles. The mutual transformations between these two sets enable the enforcement of the no-slip boundary conditions on all solid-liquid interfaces. The resulting algebraic relations provide the frequency-dependent two-body frictions, whereas inverse Fourier transform of these after adding appropriate inertial contributions yields a time-dependent mobility response. The friction and mobility values are validated in limiting cases under short-time and long-time limits. The scaling laws of these quantities are also explored as functions of the separation distance between two solid bodies, revealing important physical insight into the complicated dynamics.

DOI: [10.1103/PhysRevFluids.6.104305](https://doi.org/10.1103/PhysRevFluids.6.104305)

I. INTRODUCTION

Mutual hydrodynamic interactions between particles suspended in a viscous fluid are crucially important in colloidal dynamics and particle transport mechanisms. For example, such an effect dictates whether attracting solid species can overcome fluid-induced stretching to form clusters in shear flow [1,2]. Similarly, these interactions affect particulate motions, causing increase in diffusivity [3,4], modification in solute concentration [5,6], and change in separation patterns [5,7–11]. Especially in dense suspensions, the influence of one particle on others plays a crucial role in rheological estimations [12,13]. In nanofluids, this also impacts thermal dynamics by altering Brownian motion as the force on one submicron body not only instigates its motion but also induces flow, moving others [14,15].

For the aforementioned reasons, many past investigations have focused on the analysis of mutual interparticle hydrodynamic interactions inside a viscous fluid. Typically these studies have considered quasisteady dynamics where the time scales for temporal variations are assumed to be much larger than the viscous time scale. As a result, the methods have been developed to solve steady linearized viscous flow equations, and the resulting plethora of works are grouped as Stokesian dynamics analysis. Numerous articles over the past few decades have ultimately made this field mature [16–22].

The underlying quasisteady assumption in Stokesian dynamics is, however, not true often. For example, if suspended particles encounter high-frequency but low-amplitude shearing oscillation,

the flow interactions should be governed by a linearized but unsteady equation. The reason is that while small amplitude allows linearization due to negligible convection, high frequency makes the problem unsteady by ensuring comparable temporal and viscous time scales. More importantly, such similarity between two scales are always true in Brownian dynamics. This happens because after being instigated by a random force a Brownian particle decelerates solely due to viscous resistance, making the duration of transiency and momentum diffusion exactly the same. Thus, a proper analysis of the Brownian effect can only be achieved if quasisteady Stokesian dynamics can be extended to include unsteadiness. This is especially true for many-body dynamics where the product of Reynolds and Strouhal numbers is of the order of unity, and the interparticle distance is within a few particulate diameters. A typical moderately dense Brownian system satisfies these conditions. This is why all contemporary Brownian theories include the effect of transient inertia [23,24].

A general numerical methodology to describe such unsteady problems is gathering increasing relevance in contemporary research. Recently, suspensions of nanospheres are shown to have enhanced thermal conductivity on which the solid solutes with small volume fraction seem to have disproportional impact [14,15]. The effect can be attributed to Brownian motion where nanoparticles drag fluid during their random motion acting as multiple stirrers causing increased heat transfer. This phenomenon can only be analyzed by many-body unsteady Brownian interactions quantifying their cumulative contributions. Similarly, recent predictions based on microrheology depend on recording time-dependent random motion of submicron tracers so that viscoelastic properties can be estimated from the data [12,13]. This is especially useful for fragile samples which cannot withstand the stresses in a conventional rheometer during the measurement process. Analysis of unsteady mutual interactions between neighboring particles can improve the microrheological technology by eliminating the error induced by neighboring tracers in a multiple tracing system. This can be beneficial in two different ways for microrheology. First, if closely situated multiple bodies are tracked with proper interaction estimation, the observation time to acquire the same amount of data can be shortened, making the detection faster. Second, the correction can rectify the errors in simulations with periodic grids by quantifying the effect of neighboring cells.

Some past articles have considered unsteady dynamics among many bodies to address the aforementioned problems. These works include analysis of subdominant inertia [25], externally imposed unsteadiness [26], and interparticulate hydrodynamic interactions [27,28]. Our present paper is, however, substantially different from these earlier papers.

This article addresses the necessity of unsteady many-body simulation by generalizing the basic mathematical procedure for Stokesian dynamics. The entire formulation consists of four major steps. First, the linearized unsteady flow equation is transformed from the temporal to the frequency domain, and the time-invariant fields in Fourier space are constructed as spatial functions. Then, the resulting governing relation for spatial variations in the form of a temporally invariant but spatially dependent Brinkman equation is solved in the presence of disconnected particles using appropriate basis functions. Third, a set of algebraic relations involving unknown amplitudes of basis functions is constructed by exploiting given boundary conditions yielding frequency-dependent many-body friction coefficients. Finally, these frictions are inserted in the equation of motion to find the unsteady mobility response of all suspended bodies to an impulsive force or torque on any of these. The first two of these components are extensively discussed and validated in our earlier work [29], which presents detailed solutions of the Brinkman equation under various conditions. The current study builds on it by completing the last two steps required for simulating unsteady many-body motion.

The outlined analysis facilitates a hitherto unrealized study of two-body unsteady flow interactions. In the past, there have been investigations on time-dependent motion of a single particle. Some earlier works have also focused on solving the Brinkman equation in the context of flow in a porous medium. To best of our knowledge, the fundamental simulation of multiparticle unsteady motion, however, has not been undertaken yet.

Consequently, this paper renders two very important results. First, it provides the frequency-dependent general frictions for a two-sphere system including both self- and mutual coefficients. Second, it shows how the motion of both varies with time if any one of these is impacted by an impulsive force or torque. The friction results are validated with known Stokesian values for different interparticle separations under low frequency or a long-time limit. In contrast, the unsteady mobility response is verified in the ballistic regime under a short-time limit. Such dual validations under two opposite limits confirm the accuracy of our analysis.

Accordingly, this paper is organized in the following way. In Sec. II, we outline the relevant details of the basis function expansion and the subsequent mathematical formulation to find the frictions. Section III presents all nontrivial friction coefficients for a two-sphere system as a function of frequency for different interparticle separations. The corresponding unsteady mobility responses are shown in Sec. IV as functions of time. Finally, the article is summarized, and the conclusions are drawn in Sec. V.

II. GENERAL SOLUTION AND MATRIX FORMULATION

This paper considers unsteady flow around two spheres of radius a with center-to-center distance s . A fluid with viscosity μ and density ρ surrounds the particles, and freely extends to infinity. The liquid remains quiescent far away from the moving spheres.

The velocity in the domain is induced by force or torque on either of the spheres. These are driven in such a way that the time scale of fluctuations in the fields is comparable to momentum diffusion. On the other hand, the instigation behind the motion is mild enough to create a small velocity scale so that the nonlinear convective contribution can be neglected. Under such conditions, the hydrodynamic fields in such a system are governed by a linearized unsteady Navier-Stokes equation:

$$\frac{\partial \mathbf{v}}{\partial t} = -\nabla p + \nabla^2 \mathbf{v}, \quad \nabla \cdot \mathbf{v} = 0. \quad (1)$$

Here, \mathbf{v} is the nondimensional velocity normalized by scale v_s , and p is the nondimensional pressure normalized by $\mu v_s/a$. Also, dimensionless time t and space \mathbf{r} are normalized by a viscous temporal scale $a^2 \rho/\mu$ and characteristic geometric dimension a , respectively.

The unsteady equation in Eq. (1) is complemented by the boundary conditions at infinity and at the surface of the spheres. In our problem, we consider all hydrodynamic fields to decay far away from the particles. Also, the solid-liquid interfaces are assumed to be no slip so that the fluid at the contact assumes the velocity corresponding to the translation and rotation of the spheres.

A. Time-invariant decomposition in Fourier space

Fourier variation $\exp(i\Omega t)$ is the eigenfunction for the temporal derivative in Eq. (1). It involves nondimensional frequency Ω which is normalized by the inverse of the viscous time scale to form dimensionless spectral space. A Fourier transform in such space helps us to create time-invariant fields only dependent on spatial coordinates.

Accordingly, we expand the hydrodynamic fields in Fourier space:

$$\mathbf{v}(\mathbf{r}, t) = \int_{-\infty}^{\infty} \mathbf{v}_{\Omega}(\mathbf{r}) \exp(i\Omega t) d\Omega, \quad p(\mathbf{r}, t) = \int_{-\infty}^{\infty} p_{\Omega}(\mathbf{r}) \exp(i\Omega t) d\Omega. \quad (2)$$

The time-independent $\mathbf{v}_{\Omega}(\mathbf{r})$ and $p_{\Omega}(\mathbf{r})$ are constructed by inverse Fourier transform:

$$\mathbf{v}_{\Omega}(\mathbf{r}) = \frac{1}{2\pi} \int_{-\infty}^{\infty} \mathbf{v}(\mathbf{r}, t) \exp(-i\Omega t) dt, \quad p_{\Omega}(\mathbf{r}) = \frac{1}{2\pi} \int_{-\infty}^{\infty} p(\mathbf{r}, t) \exp(-i\Omega t) dt, \quad (3)$$

as per the orthogonality relations for sinusoidal functions.

Our strategy is to solve for $\mathbf{v}_\Omega(\mathbf{r})$ and $p_\Omega(\mathbf{r})$ enforcing both interfacial no-slip and far-field decay conditions. Combining Eqs. (2) and (1), one infers that \mathbf{v}_Ω and p_Ω satisfy

$$i\Omega\mathbf{v}_\Omega = -\nabla p_\Omega + \nabla^2\mathbf{v}_\Omega, \quad \nabla \cdot \mathbf{v}_\Omega = 0. \quad (4)$$

This is the generalized Brinkman equation with complex constant in the form of $i\Omega$ in the left-hand side of the momentum equation. We apply our recently developed solution techniques [29] for such equations to find \mathbf{v}_Ω and p_Ω around the two particles of interest.

B. Brief outline of the solution techniques for the Brinkman equation

The vector field solution for the Brinkman equation in the presence of two disconnected spheres is described in our recent article [29]. First, we expand the field solution for Eq. (4) in terms of two complete sets of basis functions in two spherical coordinates centered around the respective two particles. Then, the transformation coefficients are derived to convert the representation of the flow in one set to the other. This leads to a system of algebraic relations coupling the unknown amplitudes to the given boundary conditions. Finally, the spectrally converged values of unknown amplitudes can be obtained by inverting the matrix representing the algebraic equations with adequate number of basis functions. Our earlier work validated the aforementioned mathematical theory using detailed simulations. This solution technique also applies to the unsteady motion of two particles in an infinitely extended viscous liquid where the eigenconstant considered in the Brinkman relation is imaginary.

Following the outlined procedure, we express the time-independent field \mathbf{v}_Ω in Eq. (4),

$$\mathbf{v}_\Omega = \sum_{lms} (\alpha_{lms}^{1-} \mathbf{v}_{lms}^{1-} + \alpha_{lms}^{2-} \mathbf{v}_{lms}^{2-}), \quad (5)$$

as a linear combination of vectorially separable basis functions $\mathbf{v}_{lms}^{i\pm}$. The superscript i in $\mathbf{v}_{lms}^{i\pm}$ means that $\mathbf{v}_{lms}^{i\pm}$ are the functions of the spherical coordinates centered around the point $\mathbf{r} = \mathbf{x}_i$ which is the location of the center of the i th particle. The translational invariance of the Brinkman relation ensures

$$\mathbf{v}_{lms}^{i\pm} = \mathbf{v}_{lms}^\pm(\mathbf{r} - \mathbf{x}_i). \quad (6)$$

The extra superscript $+$ represents regular solutions which are finite at the origin of the local coordinate, but diverge at infinity. In contrast, the “ $-$ ” stands for singular functions with singularity at the origin and vanishing strength far away. For an unbounded fluid, regular solutions are not present in Eq. (5) for their unphysical infinite value at infinity. The subscripts l and m are associated to the complete set of scalar spherical harmonic functions Y_{lm} . These can be interpreted as respective quantum numbers in θ and ϕ directions for an r - θ - ϕ spherical coordinate system with $l = 1, 2, 3, \dots$ and $m = 0, \pm 1, \pm 2, \dots, \pm l$. The subscript $s = 1, 2, 3$ denotes three independent vectors to ensure the completeness of basis solutions in three-dimensional space. These are similar to Lamb’s solutions for the steady Stokes equation in the spherical coordinates. We derive them as

$$\mathbf{v}_{lm1}^\pm(\mathbf{r}_i) = \mathbf{r}_i \times \nabla \psi_{lm}^{\text{h}\pm}(\mathbf{r}_i), \quad \mathbf{v}_{lm2}^\pm(\mathbf{r}_i) = \nabla \times \mathbf{v}_{lm1}^\pm(\mathbf{r}_i), \quad \mathbf{v}_{lm3}^\pm(\mathbf{r}_i) = \frac{i}{\Omega} \nabla \psi_{lm}^{\text{PI}\pm}(\mathbf{r}_i), \quad (7)$$

where $\mathbf{r}_i = \mathbf{r} - \mathbf{x}_i$, and

$$\psi_{lm}^{\text{PI}+}(\mathbf{r}_i) = r_i^l Y_{lm}^i, \quad \psi_{lm}^{\text{PI}-}(\mathbf{r}_i) = r_i^{-l-1} Y_{lm}^i, \quad \psi_{lm}^{\text{h}+}(\mathbf{r}_i) = \frac{g_l^+(r_i)}{r_i} Y_{lm}^i, \quad \psi_{lm}^{\text{h}-}(\mathbf{r}_i) = \frac{g_l^-(r_i)}{r_i} Y_{lm}^i, \quad (8)$$

with i indicating quantities corresponding to the i th particle. So variables r_i, θ_i, ϕ_i are three spherical coordinates with the point $\mathbf{r}_i = \mathbf{x}_i$ as the center. The functions g_l^\pm can be found from the subsequent recurrence relation

$$g_l^\pm(r_i) = \left(\frac{d}{dr_i} - \frac{l}{r_i} \right) g_{l-1}^\pm(r_i), \quad (9)$$

and the initial ones are represented by

$$g_0^+(r_i) = \sinh(kr_i), \quad g_0^-(r_i) = \exp(-kr_i), \quad (10)$$

where $k = \frac{\sqrt{2\Omega}}{2}(1+i)$. After all basis functions $\mathbf{v}_{lms}^{i\pm}$ are constructed, the field solution \mathbf{v}_Ω would be completely obtained if we evaluate unknown amplitudes α_{lms}^{i-} in Eq. (5). Thus, we concentrate on finding these by applying the given boundary conditions.

C. Matrix formulation for unknown amplitudes

The unknown amplitudes α_{lms}^{i-} are obtained from the boundary conditions by constructing a set of algebraic relations in matrix form. The construction of these matrices is a three-step process.

First, we recognize any vector function on the surface of the i th particle can be expanded in terms of the following interfacial basis involving spherical harmonics:

$$\hat{\mathbf{e}}_{lm1}^i = \mathbf{r}_i \times \nabla Y_{lm}^i, \quad \hat{\mathbf{e}}_{lm2}^i = \hat{\mathbf{e}}_{r_i} Y_{lm}^i, \quad \hat{\mathbf{e}}_{lm3}^i = r_i \nabla Y_{lm}^i. \quad (11)$$

Thus, the given velocity $\mathbf{v}_i(\theta_i, \phi_i)$ on the surface of the i th sphere can be expanded as

$$\mathbf{v}_i(\theta_i, \phi_i) = \sum_{lms} [a_{lms}^i \hat{\mathbf{e}}_{lm\sigma}^i(\theta_i, \phi_i)], \quad (12)$$

where a_{lms}^i are known constants because \mathbf{v}_i is provided. Likewise, the basis functions $\mathbf{v}_{lms}^{i\pm}$ can also be expanded as a combination of $\hat{\mathbf{e}}_{lm\sigma}^i$:

$$\mathbf{v}_{lms}^{i\pm} = \sum_{\sigma} [f_{lms\sigma}^{\pm}(r_i) \hat{\mathbf{e}}_{lm\sigma}^i(\theta_i, \phi_i)]. \quad (13)$$

Here, the scalar functions $f_{lms\sigma}^{\pm}$ depend only on r_i , making these invariant of angular co-ordinates. These functions are constructed from the following relations:

$$\begin{aligned} \mathbf{v}_{lm1}^{i\pm} &= \frac{g_l^{\pm}(r_i)}{r_i} \hat{\mathbf{e}}_{lm1}^i, & \mathbf{v}_{lm2}^{i\pm} &= -\frac{l(l+1)}{r_i^2} g_l^{\pm}(r_i) \hat{\mathbf{e}}_{lm2}^i - \frac{g_l^{\pm}(r_i)}{r_i} \hat{\mathbf{e}}_{lm3}^i, \\ \mathbf{v}_{lm3}^{i+} &= l r_i^{l-1} \hat{\mathbf{e}}_{lm2}^i + r_i^{l-1} \hat{\mathbf{e}}_{lm3}^i, & \mathbf{v}_{lm3}^{i-} &= (-l-1) r_i^{-l-2} \hat{\mathbf{e}}_{lm2}^i + r_i^{-l-2} \hat{\mathbf{e}}_{lm3}^i. \end{aligned} \quad (14)$$

We realize that it is convenient to use a 3×3 matrix representation $[\mathbf{F}_{lm}^{\pm}]$,

$$[\mathbf{F}_{lm}^+] = \begin{bmatrix} \frac{g_l^+(r_i)}{r_i} & 0 & 0 \\ 0 & -\frac{l(l+1)}{r_i^2} g_l^+(r_i) & -\frac{g_l^+(r_i)}{r_i} \\ 0 & l r_i^{l-1} & r_i^{l-1} \end{bmatrix}, \quad [\mathbf{F}_{lm}^-] = \begin{bmatrix} \frac{g_l^-(r_i)}{r_i} & 0 & 0 \\ 0 & -\frac{l(l+1)}{r_i^2} g_l^-(r_i) & -\frac{g_l^-(r_i)}{r_i} \\ 0 & (-l-1) r_i^{-l-2} & r_i^{-l-2} \end{bmatrix}, \quad (15)$$

with $f_{lms\sigma}^{\pm}$ being the σ th element of the s th row in $[\mathbf{F}_{lm}^{\pm}]$.

Second, we derive a transformation matrix $[M_{ij}^{\mp}]$ which relates the two sets of basis vectors \mathbf{v}_{lms}^{i-} and \mathbf{v}_{lms}^{i+} ,

$$\mathbf{v}_{lms}^{i-} = \sum_{l'm's'} M_{lmsl'm's'}^{ij\mp} \mathbf{v}_{l'm's'}^{i+}, \quad (16)$$

for $|\mathbf{r} - \mathbf{x}_j| < |\mathbf{x}_i - \mathbf{x}_j|$. As a result, the field solution in Eq. (5) can be expressed in one single set of spherical coordinates with origin at the center of either particle. This allows us to build relations between unknown amplitudes α_{lms}^{i-} and given constants a_{lms}^i known from the boundary conditions. As a result, on the surface of the first particle, one finds

$$a_{\lambda\mu\sigma}^1 = \sum_s [\alpha_{\lambda\mu s}^{1-} f_{\lambda\mu s\sigma}^- (a_1)] + \sum_{lms'} [\alpha_{lms}^{2-} M_{lms\lambda\mu s'}^{21\mp} f_{\lambda\mu s'\sigma}^+ (a_1)]. \quad (17)$$

Similarly, the boundary condition around the second particle implies

$$a_{\lambda,\mu\sigma}^2 = \sum_s [\alpha_{\lambda,\mu\sigma}^{2-} f_{\lambda,\mu\sigma}^-(a_2)] + \sum_{lms'} [\alpha_{lms}^{1-} M_{lms\lambda,\mu\sigma}^{12\mp} f_{\lambda,\mu\sigma}^+(a_2)], \quad (18)$$

where a_i in parentheses means radius of the i th particle.

Finally, a matrix relation

$$\langle \mathbf{a} | = \langle \alpha | [\mathbf{G}] \quad (19)$$

is formed by combining Eqs. (17) and (18). Here, both $\langle \mathbf{a} |$ and $\langle \alpha |$ are row matrices containing elements $a_{\lambda,\mu\sigma}^1$, $a_{\lambda,\mu\sigma}^2$ and α_{lms}^{1-} , α_{lms}^{2-} , respectively. The amplitudes for both particles are stacked together so that the respective subsets are displayed as subrows

$$\langle \mathbf{a} | = \langle \{ a_{\lambda,\mu\sigma}^1 \}, \{ a_{\lambda,\mu\sigma}^2 \} |, \quad \langle \alpha | = \langle \{ \alpha_{lms}^{1-} \}, \{ \alpha_{lms}^{2-} \} |. \quad (20)$$

The square matrix $[\mathbf{G}]$ is the grand mobility matrix with the following substructures:

$$[\mathbf{G}] = \begin{bmatrix} [F_1^-] & [M_{12}^\mp][F_2^+] \\ [M_{21}^\mp][F_1^+] & [F_2^-] \end{bmatrix}, \quad (21)$$

where both $[F_i^\pm]$ and $[M_{ij}^\mp]$ are square submatrices. Thus, as row matrix $\langle \mathbf{a} |$ conveying boundary conditions is given, unknown amplitudes $\langle \alpha |$ are evaluated by inverting grand mobility $[\mathbf{G}]$ and postmultiplying the inverse with $\langle \mathbf{a} |$. Then, one can compute first \mathbf{v}_Ω from Eq. (5) and subsequently \mathbf{v} using Eq. (2). Thus, the computation of the hydrodynamic fields will be possible in an accurate and efficient way.

III. FREQUENCY-DEPENDENT FRICTION TENSOR

This section focuses on finding the hydrodynamic force and torque on each particle in frequency space Ω for given rectilinear and rotational motion. Accordingly, we define linear $\mathbf{u}_i(t)$ and angular $\boldsymbol{\omega}_i(t)$ velocities for the i th sphere as time-dependent vectors. Similarly, the force and torque acting on it are denoted as $\mathbf{f}_i(t)$ and $\boldsymbol{\tau}_i(t)$ as temporal functions, respectively. All these unsteady quantities are expanded as Fourier transforms:

$$\mathbf{u}_i(t) = \int_{-\infty}^{\infty} \widehat{\mathbf{u}}_i(\Omega) \exp(i\Omega t) d\Omega, \quad \boldsymbol{\omega}_i(t) = \int_{-\infty}^{\infty} \widehat{\boldsymbol{\omega}}_i(\Omega) \exp(i\Omega t) d\Omega, \quad (22)$$

and

$$\mathbf{f}_i(t) = \int_{-\infty}^{\infty} \widehat{\mathbf{f}}_i(\Omega) \exp(i\Omega t) d\Omega, \quad \boldsymbol{\tau}_i(t) = \int_{-\infty}^{\infty} \widehat{\boldsymbol{\tau}}_i(\Omega) \exp(i\Omega t) d\Omega. \quad (23)$$

Here, the following inverse Fourier transforms are used,

$$\widehat{\mathbf{u}}_i(\Omega) = \frac{1}{2\pi} \int_{-\infty}^{\infty} \mathbf{u}_i(t) \exp(-i\Omega t) dt, \quad \widehat{\boldsymbol{\omega}}_i(\Omega) = \frac{1}{2\pi} \int_{-\infty}^{\infty} \boldsymbol{\omega}_i(t) \exp(-i\Omega t) dt, \quad (24)$$

and

$$\widehat{\mathbf{f}}_i(\Omega) = \frac{1}{2\pi} \int_{-\infty}^{\infty} \mathbf{f}_i(t) \exp(-i\Omega t) dt, \quad \widehat{\boldsymbol{\tau}}_i(\Omega) = \frac{1}{2\pi} \int_{-\infty}^{\infty} \boldsymbol{\tau}_i(t) \exp(-i\Omega t) dt, \quad (25)$$

to reveal translation, rotation, force, and torque for the i th body in the frequency space.

The linearized governing equation allows superposition of solutions corresponding to individual components of the rigid-body motion. Thus, friction tensors can be constructed relating the force and torque on the pair of particles to their linear and angular velocities. Such frequency-dependent second-order friction tensors $\widehat{\mathbf{J}}_{ij}^t(\Omega)$, $\widehat{\mathbf{J}}_{ij}^r(\Omega)$, $\widehat{\mathbf{J}}_{ij}^{tr}(\Omega)$, $\widehat{\mathbf{J}}_{ij}^{rt}(\Omega)$ are defined to express $\widehat{\mathbf{f}}_i(\Omega)$ and $\widehat{\boldsymbol{\tau}}_i(\Omega)$

in terms of $\widehat{\mathbf{u}}_j(\Omega)$ and $\widehat{\boldsymbol{\omega}}_j(\Omega)$:

$$\widehat{\mathbf{f}}_i(\Omega) = \sum_j [\widehat{\mathbf{J}}_{ij}^{tt}(\Omega) \cdot \widehat{\mathbf{u}}_j(\Omega) + \widehat{\mathbf{J}}_{ij}^{tr}(\Omega) \cdot \widehat{\boldsymbol{\omega}}_j(\Omega)], \quad \widehat{\boldsymbol{\tau}}_i(\Omega) = \sum_j [\widehat{\mathbf{J}}_{ij}^{rt}(\Omega) \cdot \widehat{\mathbf{u}}_j(\Omega) + \widehat{\mathbf{J}}_{ij}^{rr}(\Omega) \cdot \widehat{\boldsymbol{\omega}}_j(\Omega)]. \quad (26)$$

Here, superscripts t and r represent quantities associated to the translational (like $\widehat{\mathbf{u}}, \widehat{\mathbf{f}}$) and rotational (like $\widehat{\boldsymbol{\omega}}, \widehat{\boldsymbol{\tau}}$) vectors. The subscripts i and j in $\widehat{\mathbf{J}}_{ij}^{PQ}$ (P, Q denotes t or r) mean the effect on the j th particle generated by motion of the i th particle. In the nondimensional formulation, $\widehat{\mathbf{J}}_{ij}^{tt}$ and $\widehat{\mathbf{J}}_{ij}^{rr}$ are interpreted as frictions normalized by μa and μa^3 , whereas both $\widehat{\mathbf{J}}_{ij}^{tr}$ and $\widehat{\mathbf{J}}_{ij}^{rt}$ are scaled with μa^2 . It is to be noted that $\widehat{\mathbf{J}}_{ij}^{rt}$ is the transpose of $\widehat{\mathbf{J}}_{ji}^{tr}$ as per reciprocal theorem. Subscript i in $\widehat{\mathbf{f}}_i$ or $\widehat{\boldsymbol{\tau}}_i$ stands for force or torque exerted on the i th particle by the fluid, while subscript j in $\widehat{\mathbf{u}}_j(\Omega)$ or $\widehat{\boldsymbol{\omega}}_j$ represents linear or angular velocity of the j th particle.

For the two-body system, there are 16 friction tensors represented by $\widehat{\mathbf{J}}_{ij}^{pq}$ where i or j both can assume the value 1 or 2 independently denoting a specific sphere, and P, Q can stand for either translation or rotation. Our goal is to evaluate all nontrivial elements in these 16 friction tensors as functions of Fourier frequency Ω . This is realized by using the following contraction, where simple superposition of force and torque from the individual basis solution is implemented:

$$\widehat{\mathbf{J}}_{ij}^{PQ} = \sum_{ls\lambda\sigma} \mathbf{v}_{ls}^{(m)P} \cdot \mathbf{G}_{ls\lambda\sigma}^{-1(m)ij} \cdot \left[\mathbf{w}_{\lambda\sigma}^{(m)Q-} + \left(\sum_{j\lambda'\sigma'} M_{\lambda\lambda'\sigma\sigma'}^{(m)jk\mp} \cdot \mathbf{w}_{\lambda'\sigma'}^{(m)Q+} \right) \right]. \quad (27)$$

Here, $\mathbf{v}_{ls}^{(m)P}$ represents the basis vectors for the given velocity associated to P -type motion as boundary conditions. In contrast, $\mathbf{w}_{\lambda\sigma}^{(m)Q-}$ or $\mathbf{w}_{\lambda'\sigma'}^{(m)Q+}$ means force (if $Q = T$) or torque (if $Q = R$) generated by the corresponding singular or regular basis function centered around the respective sphere. Detailed expressions of $\mathbf{v}_{ls}^{(m)P}$, $\mathbf{w}_{\lambda\sigma}^{(m)Q-}$, and $\mathbf{w}_{\lambda'\sigma'}^{(m)Q+}$ are articulated in the Appendix. The corresponding matrix elements in the i th, j th block in the inverse of $[\mathbf{G}]$ [see Eq. (21)] are denoted by $\mathbf{G}_{ls\lambda\sigma}^{-1(m)ij}$. Also, $M_{\lambda\lambda'\sigma\sigma'}^{(m)jk\mp}$ are coefficients in a matrix defined as $M_{jk}^{\mp}(1 - \delta_{jk})$ with δ_{jk} being the Kronecker delta.

In Eq. (27), identical spheres imply that $\widehat{\mathbf{J}}_{11}^{pq} = \widehat{\mathbf{J}}_{22}^{pq}$ as well as $\widehat{\mathbf{J}}_{12}^{pq} = \widehat{\mathbf{J}}_{21}^{pq}$ for $p=q$ and $\widehat{\mathbf{J}}_{12}^{pq} = -\widehat{\mathbf{J}}_{21}^{pq}$ for $p \neq q$. Moreover, the reciprocal theorem ensures $\widehat{\mathbf{J}}_{ij}^{pq} = \widehat{\mathbf{J}}_{ji}^{qp \dagger}$ with \dagger being conjugate transpose. We check that these obvious symmetries are satisfied by Eq. (27) and the relations in the Appendix. Thus, the nonzero components of the independent tensors are described in the subsequent narration.

A. Validation of friction coefficients with known Stokesian results

We employ Eq. (27) to calculate independent nonzero elements of $\widehat{\mathbf{J}}_{ij}^{PQ}$, and compare the results with known benchmark values according to Stokesian analysis for $\Omega \rightarrow 0$. Two different separation distances between two spheres are chosen to achieve a comprehensive validation. The comparison is presented in Table I, which reveals the accuracy of the outlined algorithm emphatically.

The symmetry of the geometry dictates that $\widehat{\mathbf{J}}_{ij}^{tt}$ and $\widehat{\mathbf{J}}_{ij}^{rr}$ are all diagonal tensors. As a result, these can be decomposed into diagonal components:

$$\widehat{\mathbf{J}}_{ij}^{tt} = \widehat{J}_{ij}^{t\perp} \widehat{\mathbf{e}}_z \widehat{\mathbf{e}}_z + \widehat{J}_{ij}^{t\parallel} (\mathbf{I} - \widehat{\mathbf{e}}_z \widehat{\mathbf{e}}_z), \quad \widehat{\mathbf{J}}_{ij}^{rr} = \widehat{J}_{ij}^{r\perp} \widehat{\mathbf{e}}_z \widehat{\mathbf{e}}_z + \widehat{J}_{ij}^{r\parallel} (\mathbf{I} - \widehat{\mathbf{e}}_z \widehat{\mathbf{e}}_z). \quad (28)$$

We refer to the eigenvalue $\widehat{J}_{ij}^{t\perp}$ or $\widehat{J}_{ij}^{r\perp}$ along the line of separation as the normal component. In contrast, the degenerated $\widehat{J}_{ij}^{t\parallel}$ or $\widehat{J}_{ij}^{r\parallel}$ in the plane tangential to the spheres at the point of minimum separation is denoted as the tangential component.

The symmetry of the system also dictates that there is only one independent nonzero element in each of the translation-rotation coupling tensors. These antisymmetric tensors are defined in two groups, (1) $\widehat{\mathbf{J}}_{11}^{tr} = \widehat{\mathbf{J}}_{22}^{tr} = \widehat{\mathbf{J}}_{11}^{tr \dagger} = -\widehat{\mathbf{J}}_{22}^{tr \dagger}$ and (2) $\widehat{\mathbf{J}}_{12}^{tr} = -\widehat{\mathbf{J}}_{21}^{tr} = \widehat{\mathbf{J}}_{21}^{tr \dagger} = -\widehat{\mathbf{J}}_{12}^{tr \dagger}$, where both can

TABLE I. Comparison between Stokesian results and computed friction values.

	For separation $s = 2.1$		For separation $s = 3$	
	Stokesian results	Friction for $\Omega = 10^{-5}$	Stokesian results	Friction for $\Omega = 10^{-5}$
$\widehat{\mathbf{J}}_{11}^t$ tangential	-26.257	-26.280	-20.280	-20.323
$\widehat{\mathbf{J}}_{11}^t$ normal	-76.003	-76.018	-25.795	-25.816
$\widehat{\mathbf{J}}_{11}^r$ tangential	-30.989	-30.990	-25.585	-25.585
$\widehat{\mathbf{J}}_{11}^r$ normal	-25.844	-25.844	-25.182	-25.182
$\widehat{\mathbf{J}}_{12}^t$ tangential	12.438	12.416	5.602	5.575
$\widehat{\mathbf{J}}_{12}^t$ normal	63.734	63.713	12.633	12.612
$\widehat{\mathbf{J}}_{12}^r$ tangential	-2.557	-2.556	-0.545	-0.544
$\widehat{\mathbf{J}}_{12}^r$ normal	2.936	2.936	0.934	0.934
$\widehat{\mathbf{J}}_{11}^r$	4.957	4.953	0.713	0.710
$\widehat{\mathbf{J}}_{12}^r$	7.755	7.760	2.330	2.333

be uniquely described by the following form:

$$\widehat{\mathbf{J}}_{ij}^r = \widehat{J}_{ij}^r \mathbf{E} \cdot \hat{\mathbf{e}}_z. \quad (29)$$

Here \widehat{J}_{ij}^r represents the antisymmetric translation-rotation coupling with \mathbf{E} being the third-order permutation tensor.

Simulated values of all nontrivial components of the mentioned tensors are displayed in Table I. We use $\Omega = 10^{-5}$ in the algorithm outlined in the current article to get one set of values. The second set of results is obtained by using well-documented Stokesian analysis [30]. The maximum relative departure between two sets is below 1%.

We check the two sets of simulations for two closely situated spheres ($s = 2.1$) as well as the moderately separated ones ($s = 3$). The former is a more difficult convergence compared to the latter. To attain the same level of accuracy, we chose maximum spectral order l_{\max} to be 32 and 16 in the frequency-dependent simulation for the respective cases. The frequency-independent Stokesian computation is especially well converged for both cases, because it complements the basis function expansion with lubrication theory. Even though the corresponding lubrication analysis is not yet available for the unsteady dynamics, the level of accuracy captured solely by basis function expansion is indeed impressive, indicating the reliability of the methodology.

The designed validation under the zero-frequency limit ensures the correct starting values for subsequent plots describing spectral variations of friction. Such dependence on frequency ultimately quantifies how much unsteady systems depart from Stokesian dynamics.

B. Translational friction tensors

The methodology is used to explore the frequency-dependent friction coefficients for a wide range of frequency Ω as well as separation distance s . We plot the independent eigenvalues of translation-translation tensors in Figs. 1 and 2 as a function of Ω for four different values of s .

In Fig. 1, the real values of tangential and normal eigenvalues of both self- and mutual translation-translation tensors are plotted. In contrast to Stokesian analysis, frequency-dependent friction tensors are complex numbers indicating an inertia-induced phase lag between force and motion. The corresponding imaginary parts of respective friction coefficients are presented in Fig. 2.

We try to find s -dependent renormalization factors for the frictions as well as for the dimensionless Ω to make renormalized curves for different s collapse into a narrow band. The dependence of such factors with separation s is displayed in each figure panel. These expressions reveal the underlying physics involving the nature of the flow dynamics.

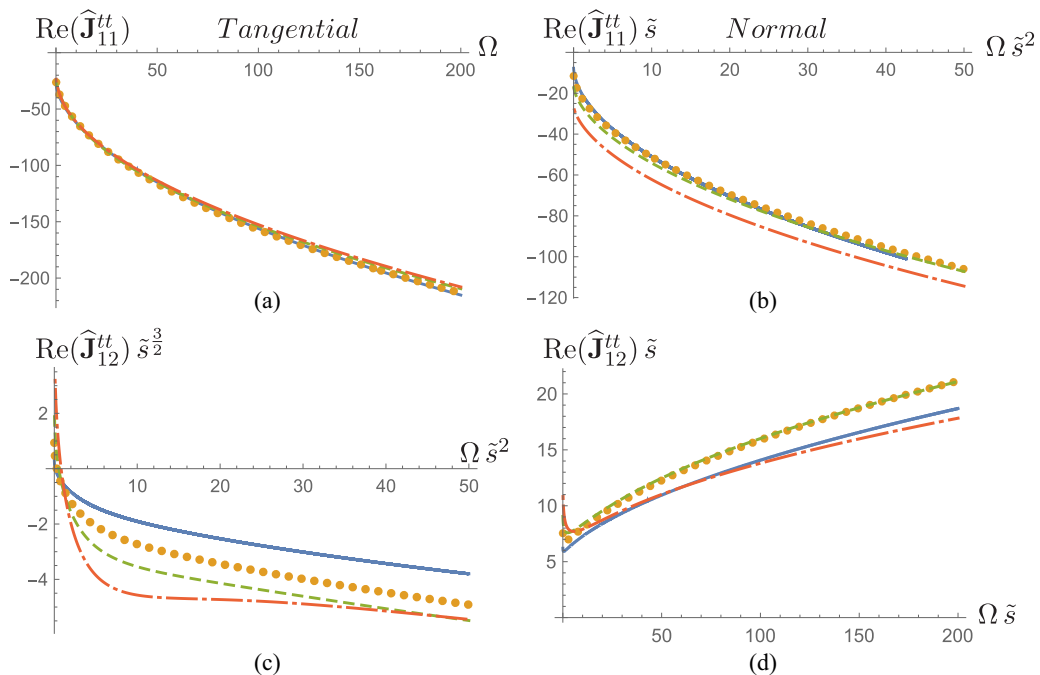


FIG. 1. Normalized nonzero real part of translational friction $\widehat{\mathbf{J}}_{11}^{tt}$ or $\widehat{\mathbf{J}}_{12}^{tt}$ is plotted as a function of natural frequency Ω under tangential (left panel) or normal (right panel) incitement with center-to-center separation $s = 2.1$ (solid line), $s = 2.25$ (dotted line), $s = 2.5$ (dashed line), and $s = 3$ (dot-dashed line). Surface-to-surface separation \tilde{s} is a renormalized factor defined as $\tilde{s} = s - 2$.

We notice that real values of friction for tangential self-translation do not require any renormalization, exhibiting the minimal effect of the neighboring sphere. It is to be noted that for quasisteady Stokesian dynamics these coefficients have a very weak logarithmic increase with decreasing surface-to-surface separation. Thus, for such quantities, the flow induced in the inertial boundary layer outside the lubrication region is mainly responsible for creating the resistance. Also, one can notice that the self-friction is consistently negative, as the viscous effect has to be purely resistive. It increases with frequency due to the creation of hindering fields caused by the fluid inertia in the boundary layer manifesting Basset history force. This effect increases proportionally to $\sqrt{\Omega}$ for high excitation frequencies because then the Basset contribution scales as $\mu a^2/l_{md}$ with $l_{md} = a/\sqrt{\Omega}$ being the length scale for momentum diffusion. The lack of variations with s as well as curvatures in the plots make the expected proportionality with $\sqrt{\Omega}$ evident in Fig. 1.

The spectral dependence of normal self-friction is similar to the corresponding tangential component except in the low-frequency Stokesian limit. For very slow oscillations, the main contribution in hydrodynamic resistance appears due to viscous effects in the lubrication region at the narrowest gap between the two spheres. Such Stokesian friction in nondimensional form scales as $a/(s - 2a) = 1/(\tilde{s})$ [31]. Thus, we rescale the normal eigenvalue of \mathbf{J}_{11}^{tt} by multiplying with \tilde{s} . For the high-frequency regime, however, the inertial Basset scaling dictates a proportionality to $\sqrt{\Omega}$. We can restore this expected behavior by renormalizing Ω by its product with \tilde{s}^2 . As a result, one can see that the curves for normal self-friction collapsed properly in Fig. 1 irrespective of separation values.

Unlike self-frictions, the mutual tangential friction is positive for low frequencies, showing how one body can be dragged by the other in the direction of its motion in accordance to the Stokesian dynamics. The mutual coefficients, however, become negative for larger frequency, when

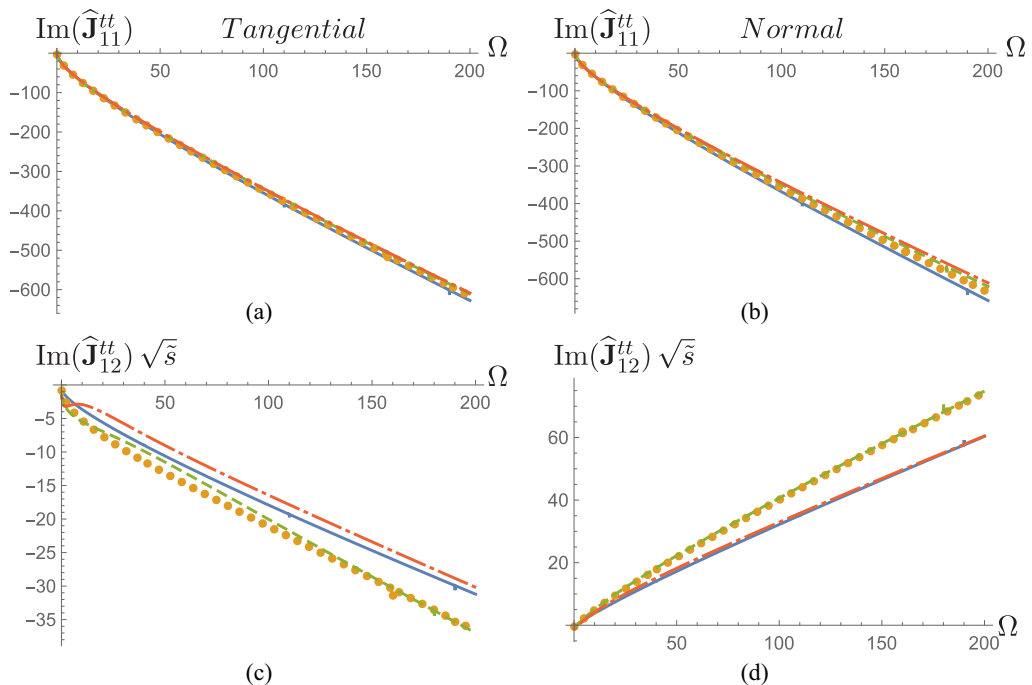


FIG. 2. Normalized nonzero imaginary part of translational friction $\hat{\mathbf{J}}_{11}^{tt}$ or $\hat{\mathbf{J}}_{12}^{tt}$ is plotted as a function of natural frequency Ω under tangential (left panel) or normal (right panel) incitement with center-to-center separation $s = 2.1$ (solid line), $s = 2.25$ (dotted line), $s = 2.5$ (dashed line), and $s = 3$ (dot-dashed line). Surface-to-surface separation \tilde{s} is a renormalized factor defined as $\tilde{s} = s - 2$.

inertia-induced recirculating fields become stronger for quicker fluctuations. Such an effect remains proportional to $\sqrt{\Omega/\tilde{s}}$ with the factor $\sqrt{1/\tilde{s}}$ being multiplied to Basset scaling $\sqrt{\Omega}$ to account for the impact of particulate separations on mutual interactions. We notice that the interplay between the direct viscous stress and the opposing inertial field flip the curves to negative value at a crossover frequency scaled with \tilde{s} . One should note that the nondimensional Ω is obtained by multiplying the nominal time scale $a^2\rho/\mu$ with excitation frequency, where the natural length scale is assumed as a . The introduction of the renormalization of Ω by multiplying with \tilde{s} reveals a new time scale in the form of $a(s-2a)\rho/\mu$ indicating a new length scale $\sqrt{a(s-2a)}$ for the problem. We immediately recognize this new dimension as the radial extent of the lubrication domain in between two bodies manifesting the enhanced importance of the near-contact region. This implies that the interplay between the lubrication dynamics and the inertia-induced fields outside the contact region dictates the behavior of the mutual influence in the tangential direction. When the aforementioned renormalization of the abscissa is coupled to a multiplicative factor of $\tilde{s}^{3/2}$ to the ordinate, proportionality to $\sqrt{\Omega/\tilde{s}}$ for large Ω can be captured. This fact is attested by Fig. 1, where the curves are grouped together closely except the purely Stokesian values at $\Omega = 0$.

The normal translational mutual friction does not show any crossover—it is always positive, indicating the thrust created by the moving body on the static one. In absence of any crossover, we use lubrication scaling $1/\tilde{s}$ for normal motion to rescale the frictional coefficient by multiplying it by \tilde{s} . Then, the high-frequency Basset contribution requires the abscissa to be multiplied by \tilde{s} so that proportionality to $\sqrt{\Omega/\tilde{s}}$ is properly represented. Such replotting immediately produced closely clustered curves.

The competitive interplay between inertia and viscous lubrication is subdued in Fig. 2, as the imaginary part of the friction only appears due to the former for an unsteady system. This is why all

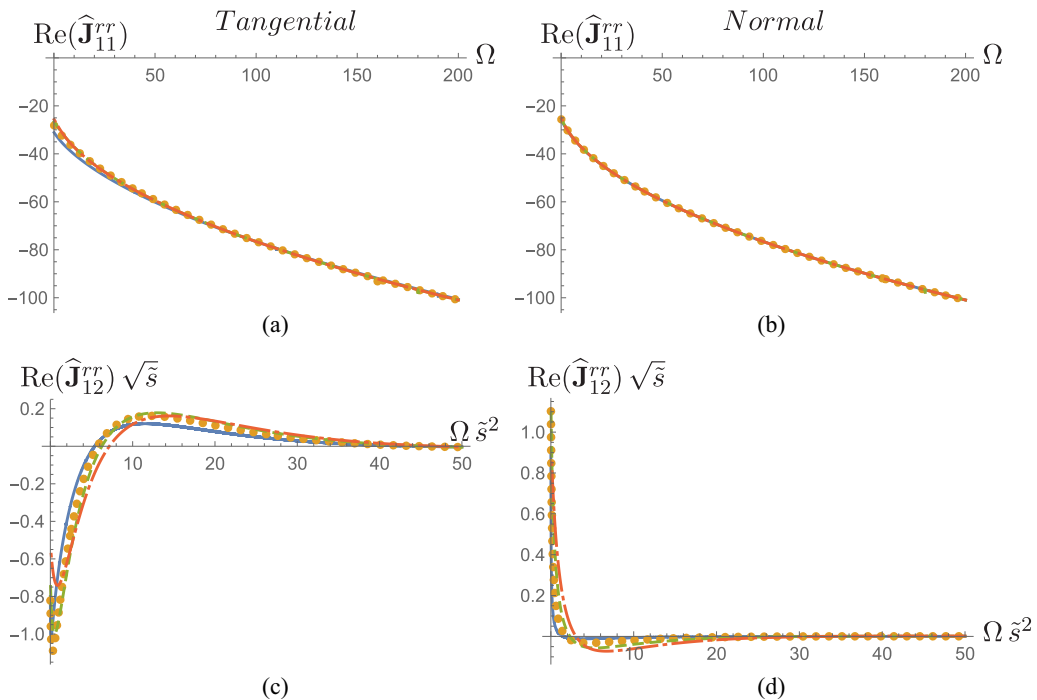


FIG. 3. Normalized nonzero real part of rotational friction $\widehat{\mathbf{J}}_{11}^r$ or $\widehat{\mathbf{J}}_{12}^r$ is plotted as a function of natural frequency Ω under tangential (left panel) or normal (right panel) incitement with center-to-center separation $s = 2.1$ (solid line), $s = 2.25$ (dotted line), $s = 2.5$ (dashed line), and $s = 3$ (dot-dashed line). Surface-to-surface separation \tilde{s} is a renormalized factor defined as $\tilde{s} = s - 2$.

the curves approach zero when $\Omega \rightarrow 0$ in Fig. 2. For finite Ω , the imaginary part of the self-friction is most affected by the fluid acceleration especially in the boundary layer around the entire sphere. This effect akin to the “added mass term” is proportional to Ω irrespective of s explaining closely grouped straight line plots for self-elements in Fig. 2. The boundary layer around the entire sphere is not, however, important when the sphere is not moving. Then, the part of this layer inside the contact region predominantly affects force on the static body. Thus, the imaginary part of mutual friction grows relatively more with the increasing proximity to the moving sphere. Such increase is represented by the product of the nondimensional friction and $\sqrt{\tilde{s}}$ in Fig. 2. The positivity and negativity of the quantities in Fig. 2 are consistent with Fig. 1, implying proper satisfaction of causality.

C. Rotational friction tensors

We present independent eigenvalues of rotational frictions in Figs. 3 and 4. In Fig. 3, their real parts are plotted, whereas Fig. 4 displays the imaginary parts. All plots are renormalized with appropriate s -dependent factors to ensure the coherent collapse of the curves.

As seen for the tangential self-translational tensor in Fig. 2, real parts of both eigenvalues of rotational counterparts do not need any renormalization of either the abscissa or the ordinate. This means that viscous stresses in the lubrication region have a weaker impact on self-rotational resistance. On the contrary, the main contribution in $\widehat{\mathbf{J}}_{11}^r$ comes from the Basset history caused by the inertial boundary layer over the entire sphere. As a result, the simulated results for $\widehat{\mathbf{J}}_{11}^r$ exhibit negligible variation with s as well as proportionality to $\sqrt{\Omega}$ for large frequency. Also, their negative values manifest the resistive nature of the surrounding fluid.

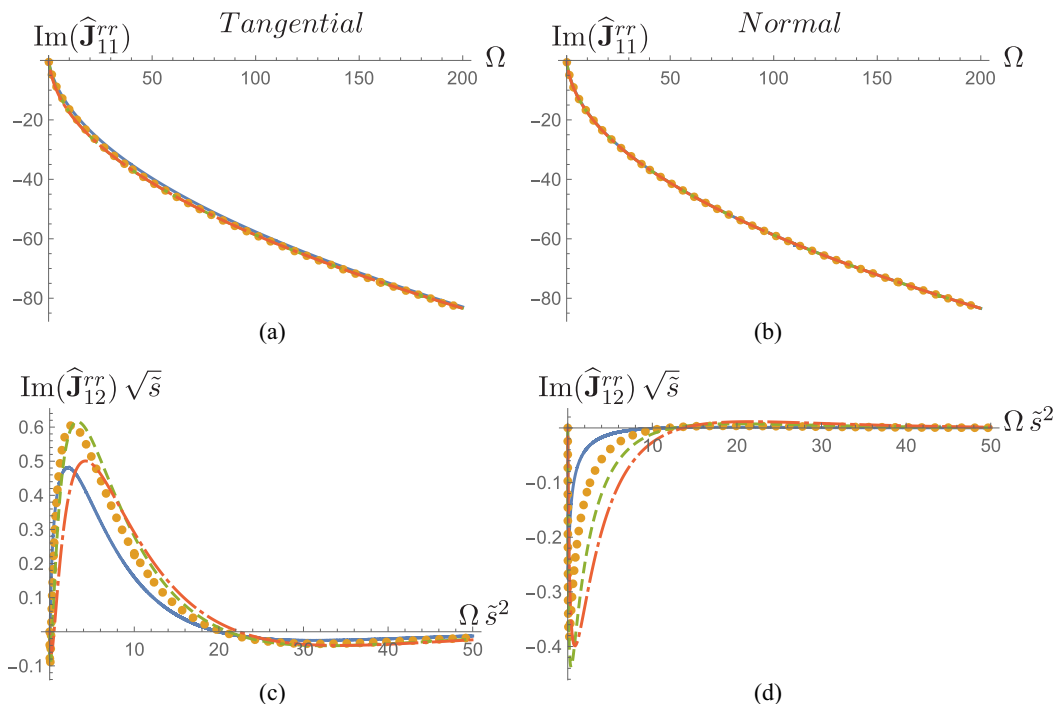


FIG. 4. Normalized nonzero imaginary part of rotational friction $\widehat{\mathbf{J}}_{11}^{rr}$ or $\widehat{\mathbf{J}}_{12}^{rr}$ is plotted as a function of natural frequency Ω under tangential (left panel) or normal (right panel) incitement with center-to-center separation $s = 2.1$ (solid line), $s = 2.25$ (dotted line), $s = 2.5$ (dashed line), and $s = 3$ (dot-dashed line). Surface-to-surface separation \tilde{s} is a renormalized factor defined as $\tilde{s} = s - 2$.

The mutual rotational frictions, however, require renormalizations of both the abscissa and the ordinate. The rescaling factor for Ω is \tilde{s}^2 , indicating a new time scale $(s-2a)^2 \rho/\mu$ or a characteristic length as surface-to-surface separation $(s-2a)$. This implies the importance of the direct viscous interactions in the lubrication region to be the primary mechanism responsible for transmission of torque from the rotating sphere to the static one. As a result, both components of mutual rotational friction recover a renormalization factor which should be a logarithmic function of \tilde{s} according to lubrication theory. We find such factor a little problematic to handle as it goes to zero for $s = 3a$. Thus, we choose a function weaker than $1/\tilde{s}$ to multiply with the ordinate leading to a reasonable clustering of the curves.

Both mutual components display an interplay between viscous interactions in the lubrication region and Basset contribution from the inertial boundary layer in the same location. The former, being stronger in the Stokes regime, tries to drive the fixed sphere following the motion of the driver at the near-contact point. The latter, however, grows larger for higher frequencies, and creates an opposing effect due to inertia-generated fields. Such counterbalancing dynamics is evident in Fig. 3, where all curves for mutual rotational friction change sign.

For rotational motions, the phase lag between the torque and the angular velocity is mainly caused by the Basset term, as added mass is irrelevant for axisymmetric revolution. Accordingly, one can see the similarity between the real and imaginary parts of the rotational frictions for high-frequency values as described by Figs. 3 and 4, respectively. For low frequencies, the imaginary parts vanish predictively as evident in Fig. 4. It is obvious from Fig. 4 that the imaginary parts of the self-rotation friction are caused by the entire inertial layer across the spherical surface. On the contrary, the same for the mutual one is most influenced by the acceleration-induced fields at the contact region.

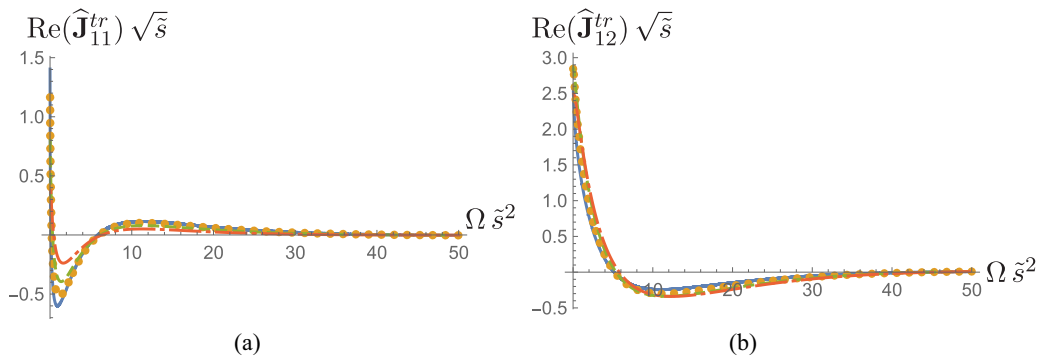


FIG. 5. Normalized nonzero real part of translation-rotation friction $\widehat{\mathbf{J}}_{11}^{tr}$ or $\widehat{\mathbf{J}}_{12}^{tr}$ is plotted as a function of natural frequency Ω with center-to-center separation $s = 2.1$ (solid line), $s = 2.25$ (dotted line), $s = 2.5$ (dashed line), and $s = 3$ (dot-dashed line). Surface-to-surface separation \tilde{s} is a renormalized factor defined as $\tilde{s} = s - 2$.

D. Translation-rotation couplings

In Figs. 5 and 6, the real and the imaginary parts of the only independent component in antisymmetric translation-rotation coupling tensors are presented. Both the self- and the mutual frictions are plotted as functions of frequency for different separations in these figures. Like translational and rotational frictions, the renormalization factors for proper collapse of the curves are indicated in the plots.

In both Figs. 5 and 6, the renormalization of the frequency implies that the translation-rotation coupling occurs due to direct viscous as well as inertial interactions in the near-contact region. This is an expected conclusion as rotation can generate force only in the presence of a neighboring particle in close proximity. As a result, the curves in Figs. 5 and 6 have qualitative similarities with mutual rotational frictions in Figs. 3 and 4, respectively.

IV. TIME-DEPENDENT MOBILITY RESPONSE

The frequency-dependent frictions presented in Sec. III imply a delayed action of motion-instigating quantities like force and torque on the particulate dynamics. This means that if any

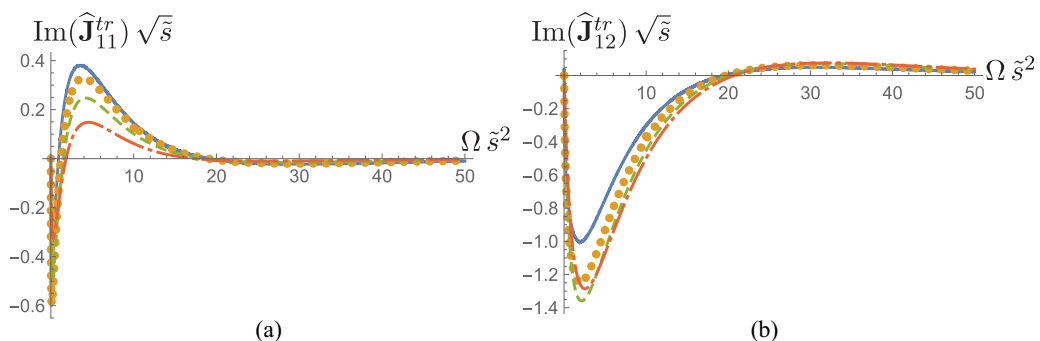


FIG. 6. Normalized nonzero imaginary part of translation-rotation friction $\widehat{\mathbf{J}}_{11}^{tr}$ or $\widehat{\mathbf{J}}_{12}^{tr}$ is plotted as a function of natural frequency Ω with center-to-center separation $s = 2.1$ (solid line), $s = 2.25$ (dotted line), $s = 2.5$ (dashed line), and $s = 3$ (dot-dashed line). Surface-to-surface separation \tilde{s} is a renormalized factor defined as $\tilde{s} = s - 2$.

solid body encounters an impulse in an inertial viscous fluid, its motion depends not only on the instantaneous force or torque but also on their history. Such retarded response can be expressed by following convolutions:

$$\mathbf{u}_i(t) = \int_0^t \left\{ \sum_j [\mathbf{K}_{ij}^{tt}(t_0) \cdot \mathbf{f}_j^e(t-t_0) + \mathbf{K}_{ij}^{tr}(t_0) \cdot \boldsymbol{\tau}_j^e(t-t_0)] \right\} dt_0, \quad (30)$$

and

$$\boldsymbol{\omega}_i(t) = \int_0^t \left\{ \sum_j [\mathbf{K}_{ij}^{rt}(t_0) \cdot \mathbf{f}_j^e(t-t_0) + \mathbf{K}_{ij}^{rr}(t_0) \cdot \boldsymbol{\tau}_j^e(t-t_0)] \right\} dt_0. \quad (31)$$

Here, \mathbf{f}_j^e and $\boldsymbol{\tau}_j^e$ represent given external force and torque exerted on the j th particle, whereas $\mathbf{K}_{ij}^{pq}(t)$ are time-dependent mobility tensors.

In this section, we compute unsteady mobility tensors \mathbf{K}_{ij}^{pq} as temporal functions describing motions due to a force or a torque proportional to the Dirac delta function in time. The simulations consider four different initial separations between two particles of interest. As a result, one can estimate how a Brownian sphere moves in the presence of others, when instigated by an impulsive force or torque in the presence of fluid inertia. It also shows how it creates flow fields around its vicinity to affect a neighboring suspended solid over time.

A. Construction of physical mobility matrix

The Fourier transforms of Eqs. (30) and (31) yield the following relations:

$$\hat{\mathbf{u}}_i(\Omega) = \sum_j [\hat{\mathbf{K}}_{ij}^{tt}(\Omega) \cdot \hat{\mathbf{f}}_j^e(\Omega) + \hat{\mathbf{K}}_{ij}^{tr}(\Omega) \cdot \hat{\boldsymbol{\tau}}_j^e(\Omega)] \quad (32)$$

and

$$\hat{\boldsymbol{\omega}}_i(\Omega) = \sum_j [\hat{\mathbf{K}}_{ij}^{rt}(\Omega) \cdot \hat{\mathbf{f}}_j^e(\Omega) + \hat{\mathbf{K}}_{ij}^{rr}(\Omega) \cdot \hat{\boldsymbol{\tau}}_j^e(\Omega)]. \quad (33)$$

Here, $\hat{\mathbf{K}}_{ij}^{pq}$ is the frequency-dependent amplitude obtained from time-dependent \mathbf{K}_{ij}^{pq} in Fourier space, whereas $\hat{\mathbf{f}}_j^e$ and $\hat{\boldsymbol{\tau}}_j^e$ are the same for \mathbf{f}_j^e and $\boldsymbol{\tau}_j^e$. The equalities in Eqs. (32) and (33) are derived using the property stating that transformed convolution is a product of transformations.

The force or torque balance equations for each sphere relate motion-inducing and motion-defining quantities in an alternative way. Accordingly,

$$m_i \frac{d\mathbf{u}_i(t)}{dt} = \mathbf{f}_i(t) + \mathbf{f}_i^e(t), \quad L_i \frac{d\boldsymbol{\omega}_i(t)}{dt} = \boldsymbol{\tau}_i(t) + \boldsymbol{\tau}_i^e(t), \quad (34)$$

where m_i and L_i stand for mass and moment of inertia of the i th spherical particle, respectively. Also, \mathbf{f}_j and $\boldsymbol{\tau}_j$ are the viscous force and torque already defined in Eq. (23).

As a result, the Fourier transform of Eq. (34) along with Eq. (26) ensures

$$\sum_j [\{i\Omega m_i - \hat{\mathbf{J}}_{ij}^{tt}(\Omega)\} \cdot \hat{\mathbf{u}}_j(\Omega) - \hat{\mathbf{J}}_{ij}^{tr}(\Omega) \cdot \hat{\boldsymbol{\omega}}_j(\Omega)] = \hat{\mathbf{f}}_i^e(\Omega), \quad (35)$$

$$\sum_j [-\hat{\mathbf{J}}_{ij}^{rt}(\Omega) \cdot \hat{\mathbf{u}}_j(\Omega) + \{i\Omega L_i - \hat{\mathbf{J}}_{ij}^{rr}(\Omega)\} \cdot \hat{\boldsymbol{\omega}}_j(\Omega)] = \hat{\boldsymbol{\tau}}_i^e(\Omega). \quad (36)$$

We recognize that Eqs. (32) and (33) are exactly equivalent to Eqs. (35) and (36). The former set of linear relations can be obtained by simply inverting the latter set. Accordingly, we invert the linear relations in Eqs. (35) and (36) to find the frequency-dependent mobility tensors $\hat{\mathbf{K}}_{ij}^{pq}$. Finally, the

inverse Fourier transform of $\hat{\mathbf{K}}_{ij}^{pq}$ renders the time-dependent mobility response tensor

$$\mathbf{K}_{ij}^{pq}(t) = \frac{1}{2\pi} \int_{-\infty}^{\infty} \hat{\mathbf{K}}_{ij}^{pq}(\Omega) \exp(i\Omega t) d\Omega, \quad (37)$$

which also represents the motions instigated by impulsive force or torque.

The nondimensional mass m_i and momentum inertia L_i for spheres are $(4\pi/3)\bar{\rho}$ and $(8\pi/15)\bar{\rho}$ with $\bar{\rho}$ being the ratio of densities of the suspended solids and the surrounding fluids. In our simulation, we consider neutrally buoyant particles with the exact same density of the liquid inferring $\bar{\rho} = 1$. We construct the linear relations in Eqs. (35) and (36) accordingly, and invert it to compute $\hat{\mathbf{K}}_{ij}^{pq}$. Then, Eq. (37) is used to find the nonzero normal and tangential eigencomponents of the mobility response tensors as functions of time.

The presented plots provide answers to outstanding questions in particulate hydrodynamics by showing when and to what extent unsteady inertial effects are significant in many-body dynamics. We choose the temporal range along the abscissa based on the duration in which transiency is important. Such a period is dictated by the saturation of the curves to zero. This implies the validity of Stokesian dynamics after the time displayed in the subsequent figures. It is to be noted though that a purely noninertial Stokesian dynamics cannot handle impulses. Thus, the connection between the presented results under the action of impulses and noninertial viscous systems should be interpreted in an integral sense. In other words, the area under the curves produced here by δ -function force or torque is the same as the Stokesian mobility under constant instigations. Consequently, when our time-dependent curves saturate to zero beyond the displayed range, unsteady contributions do not create any major impact on the motion.

B. Translational response tensors revealing delayed action

The eigenvalues of the translation-translation mobility response tensor in tangential and normal directions are plotted in Fig. 7 as functions of time. These represent the rectilinear velocity for both spheres induced by a force impulse on one of them. The transient rate of translation of the particle interacted with the impulse is referred as self-mobility, whereas the same for the other is called mutual response. Thus, the components for both the self- and mutual tensors are presented in Fig. 7 for four different separation distances between the two particles.

As expected, the self-response is a consistently decaying temporal function suggesting that the impact of a past impulse would gradually wane. The effect of the other sphere on self-mobility is not pronounced, though a closer proximity to it exhibits less velocity. This decrease is understandable as the second sphere always tries to constrict the motion of the first. The normal component is more affected by the other body due to a head-on interaction causing stronger lubrication resistance.

For mutual response, the temporal variation is not monotonic. The associated curves always start from zero at the initial time when the impact of the impulse has not been transmitted via the fluid medium to the neighboring particle. The starting value is not apparent in Fig. 7 simply because the quantity reaches nonzero values in a very short time. The normal component first increases, when the flow induced in the fluid takes time to reach the other particle. Then, it starts to decrease in a similar manner seen for the self-components. As the normal component is created by a head-on interaction, it remains positive, always implying the neighboring sphere is directly driven by the instigated particle. In contrast, the tangential component of the mutual tensor is initially negative, meaning that at the start, the recirculating fluid ensuring volumetric conservation drives the neighbor backward. However, soon the fluid starts to circumvent the solid bodies at a greater distance, causing a similar motion between the driver and the driven. At this time, mutual tangential components flip sign to become positive. For both components, a more closely situated configuration creates more pronounced impact on the driven.

When time tends to zero, the self-friction approaches a value $1/(2\pi)$. This can be predicted from the instantaneous effect of force impulse on immediate ballistic motion. For translation of a neutrally buoyant sphere, its mass $4\pi/3$ is complemented by an added mass $2\pi/3$ from fluid,

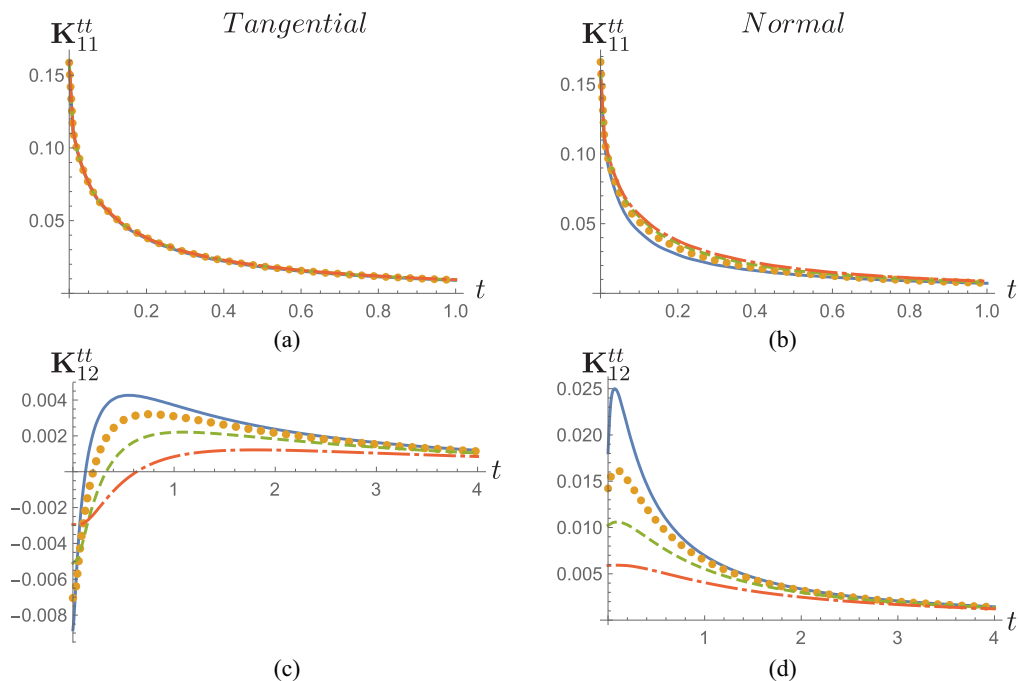


FIG. 7. Normalized nonzero translational mobility \mathbf{K}_{11}^{tt} or \mathbf{K}_{12}^{tt} is plotted as a function of time under tangential (left panel) or normal (right panel) incitement with center-to-center separation $s = 2.1$ (solid line), $s = 2.25$ (dotted line), $s = 2.5$ (dashed line), and $s = 3$ (dot-dashed line).

causing the net inertia to be 2π . A unit impulse then should produce a velocity of $1/(2\pi)$ which is replicated by the simulation. Such corroboration proves the accuracy of the presented algorithm in the short-time range, whereas the validations in Sec. III A correspond to large temporal scales. Thus, the two complementary sets of quantitative verification in two different regimes vouch for the correctness and versatility of the methodology.

C. Transient rotational response

In Fig. 8, the eigencomponents of rotation-rotation mobility response in tangential and normal directions are plotted as functions of time. This shows how angular velocity is induced for both particles when one of them encounters an impulsive unit torque. Accordingly, Fig. 8 describes both the self- and mutual mobility tensors. Like in Fig. 7, the results are presented for four different separation distances.

If Figs. 7 and 8 are compared, the corresponding plots are qualitatively very similar. The self-rotational mobility response decays monotonically with time, and shows negligible relative variations for interparticle separation distance. In contrast, the mutual rotational tensor components show first increasing and then decreasing temporal variations with zero being the starting value. One significant difference between translational and rotational mutual response is a longer time needed by the latter for reaching a maximum value signifying a slower development of recirculating flow.

For time tending to zero, the simulated results show the self-rotational mobility to be 0.5972. This value approximately matches with $15/(8\pi)$ which is the inverse of the nondimensional moment of inertia, L_i , for neutrally buoyant particles. It is to be noted that for rotational motion there is no additional inertia due to fluid as seen for translation in the form of added mass. Thus, it is expected that the angular velocity created by an impulse of unit torque will be $1/L_i$ which is corroborated by the simulation. As discussed for translational dynamics, this validation for rotational mobility under

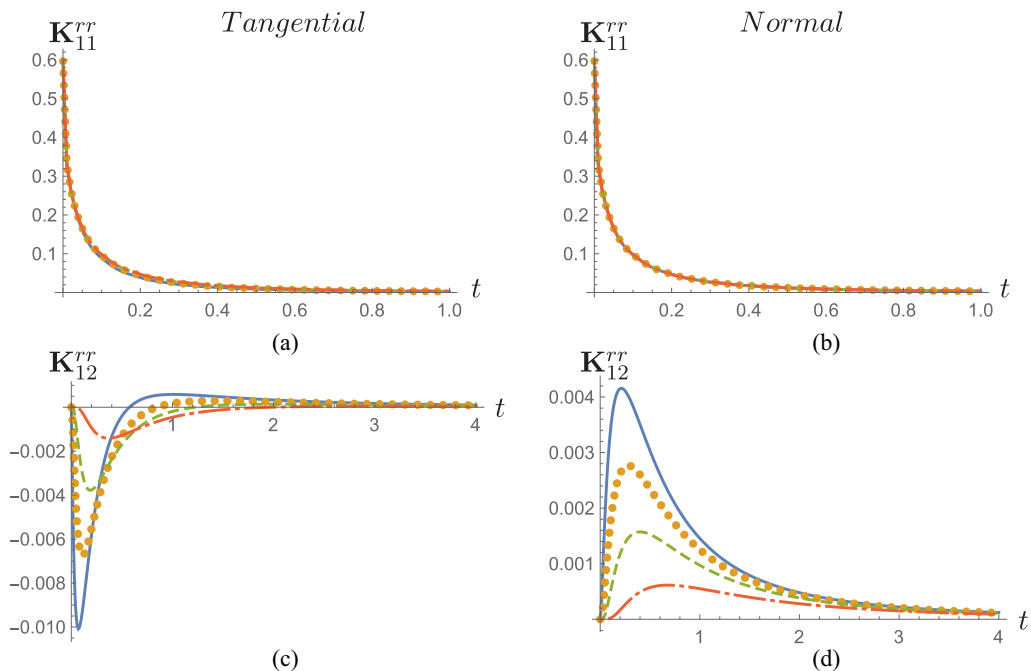


FIG. 8. Normalized nonzero rotational mobility \mathbf{K}_{11}^{rr} or \mathbf{K}_{12}^{rr} is plotted as a function of time under tangential (left panel) or normal (right panel) incitement with center-to-center separation $s = 2.1$ (solid line), $s = 2.25$ (dotted line), $s = 2.5$ (dashed line), and $s = 3$ (dot-dashed line).

the short-time limit provides additional confidence in the versatility and accuracy of the presented algorithm.

D. Unsteady translation-rotation mobility coupling

For two-body systems in fluid, an impulsive tangential force on one particle can produce delayed rotation of both. Conversely, an impulsive tangential torque can cause rectilinear motion. Such phenomena are described in Fig. 9 by the translation-rotation coupling response \mathbf{K}_{pq}^{tr} or \mathbf{K}_{pq}^{rt} .

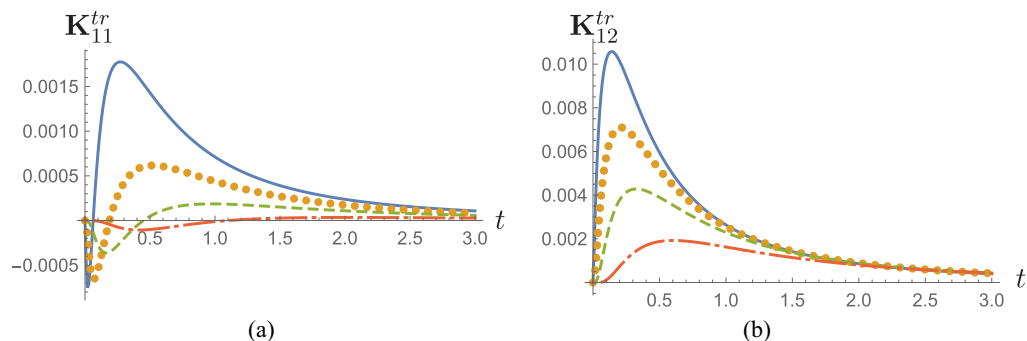


FIG. 9. Normalized nonzero translation-rotation mobility \mathbf{K}_{11}^{tr} or \mathbf{K}_{12}^{tr} is plotted as a function of time with center-to-center separation $s = 2.1$ (solid line), $s = 2.25$ (dotted line), $s = 2.5$ (dashed line), and $s = 3$ (dot-dashed line).

Due to geometric symmetry, \mathbf{K}_{pq}^{tr} and \mathbf{K}_{pq}^{rt} are antisymmetric matrices like the friction counterparts \mathbf{J}_{pq}^{tr} and \mathbf{J}_{pq}^{rt} with axis of symmetry being the direction of eigenvalue zero. Moreover, the reciprocal theorem ensures that \mathbf{K}_{pq}^{tr} is the transpose of \mathbf{K}_{qp}^{rt} . Our simulation results independently verify these relations. Thus, the translation-rotation coupling can be uniquely described by one self-function K_{11}^{tr} and one mutual one K_{12}^{tr} . These two quantities are plotted in Fig. 9 for four different separation distances.

Translation-rotation coupling appears purely due to the mutual interactions, as this effect disappears for an isolated single sphere in free space. Consequently, both plots in Fig. 9 exhibit qualitative similarity with the mutual mobility responses seen in Figs. 7 and 8. Initially, all curves in Fig. 9 start from zero because the presence of the second particle would not be felt until the fluid transmits the field. Then, the self-coefficient would initially become negative as the majority of the recirculation has to occur through the region not constricted by the neighboring solid body. In the later time, however, the recirculation zone expands beyond the particulate dimension, so that the pair can rotate as a group, causing a reversal in K_{11}^{tr} . In contrast, K_{12}^{tr} is always positive, manifesting how the driven body rotates in sync with the translation of the driver.

V. SUMMARY AND CONCLUDING REMARKS

This article presents a methodology to analyze time-dependent hydrodynamic interactions among many solid spheres in a viscous fluid. The formulation accounts for both transient inertia as well as viscous stresses, while it ignores nonlinear convective acceleration assuming low Reynolds number. The consequent linearized but unsteady Navier-Stokes equation is solved to compute the fields inside the infinite fluid domain in the presence of solid spheres. The ultimate goal of the analysis is to find the motions of all particles as temporal functions when one of these is instigated by a time-dependent force or torque.

The aforementioned analysis is completed in a four-step mathematical procedure. First, the hydrodynamic fields are expanded in separable forms with temporal Fourier functions and time-invariant but spatially varying eigensolutions for the Brinkman equation. Then, transformations between two sets of such spatially dependent eigenfunctions centered at two different spheres are derived. Third, the provided boundary conditions are exploited to form a set of algebraic relations from which the frequency-dependent friction tensors are constructed. Finally, the computed frictions are inserted into the equation of motion for translation and rotation of each sphere to describe their transient motion in terms of mobility response tensors.

The discussed algorithm is used to compute the delayed motion of two spheres when one of these has encountered an impulsive force or torque in an earlier time. Both particles are assumed to satisfy no-slip boundary conditions at their solid-liquid interfaces. These are considered to be neutrally buoyant with the exact same density as the surrounding liquid. Our simulation results include the frequency-dependent self- and mutual frictions which give the force or torque on a moving sphere as well as on a fixed neighbor, respectively. Also, the unsteady self- and mutual mobilities are computed to show how an impulse can directly make a particle move or indirectly induce motion of a neighbor via the medium.

We validate our computation by using two different known results for two mutually exclusive regimes. First, the friction coefficient under the limit of low frequency is verified by benchmark Stokesian dynamics findings. Second, the initial motion induced immediately after the action of a force or torque impulse is checked by considering particle inertia and added mass due to the fluid flow. Both tests show our simulation to be accurate with relative error around 0.1%. The first validation corresponds to long-time behavior, whereas the second one vouches for the accuracy in description of the short-time dynamics. Thus, such mutually independent verifications exhibit the robustness and versatility of the outlined algorithm.

The frequency-dependent frictions presented in this paper reveal the underlying physics of the flow dynamics. To capture this, we plot frictions as functions of frequency for different interparticle distance. Then, both abscissa and ordinate are renormalized by factors dependent on the separation

width so that the curves collapse into narrow bands. The renormalization factors for both x and y axes indicate what effect is the predominant contributor in what frequency. As expected, we see that low-frequency values of real parts in the self-resistances are mainly impacted by viscous stresses especially at the narrowest gap between two bodies. The corresponding high-frequency behaviors are, however, dictated by Basset history force due to fluid inertia around the particles. We have also seen that spectral variations in the imaginary parts of these quantities can be explained by extra inertia caused by added mass of the liquid domain. Such inertial effects are typically manifested by negligible dependence on separation distance and monotonic power-law variation with frequency. Interestingly, more complicated interplay between viscous and inertial effects can be observed in the coefficients which appear only due to the presence of a neighboring second particle. Accordingly, one can see nonmonotonic curves for mutual tensors as well as in translation-rotation coupling parameters. The opposing contributions from direct lubrication and inertia-induced recirculating fields often create reversal in these quantities as evident in their plots.

The spectral variations in friction has corresponding ramifications in temporal dependence of mobility responses. This is why one can see gradual and consistent decrease in translational and rotational self-mobilities indicating the waning impact of an initial impulse. The other coefficients only appearing due to the second sphere show an initial increase, indicating delayed transmission through the fluid medium. Then, a subsequent decay manifests the dissipation of the initial agitation. The previously mentioned interplay between the direct lubrication stresses and inertia-induced recirculation also causes reversal in sign for some of these quantities.

The developed algorithm to analyze many-body unsteady hydrodynamic interactions would be a crucial tool in a number of contemporary fluid mechanical studies. This can be immediately used to quantitatively predict nanofluidic properties by accounting for the cumulative microscopic flow fluctuations induced by many Brownian bodies. Also, one can apply our methodology to estimate the correction needed in microrheological theory, if multiple tracer particles affect each other. Similarly, filtration simulations in an inhomogeneous porous medium with large obstacles and porous matrix can import the presented formulation. We are planning to explore and expand such a wide range of fields in the near future with the mathematical procedure narrated in this article.

The data that support the findings of this study are available from the corresponding author upon reasonable request.

ACKNOWLEDGMENT

This work is supported by NSF Grant No. 1805930.

APPENDIX: VECTORS TO CONVERT FROM FUNCTIONAL TO PHYSICAL SPACE

This Appendix describes vectors $\mathbf{v}_{ls}^{(m)P}$, $\mathbf{w}_{\lambda\sigma}^{(m)Q-}$, and $\mathbf{w}_{\lambda'\sigma'}^{(m)Q+}$ in Eq. (27) for all possible indices. The three quantities require three different sets of derivations.

First, we focus on the expression of velocity $\mathbf{v}_{ls}^{(m)P}$ which is simply identified from the specified boundary condition corresponding to the considered motion. For translation of a sphere, there only exist six nonzero elements in $\mathbf{v}_{ls}^{(m)r}$, which are given by

$$\mathbf{v}_{12}^{(1)r} = \mathbf{v}_{13}^{(1)r} = -\frac{1}{2}\hat{\mathbf{e}}_x + \frac{i}{2}\hat{\mathbf{e}}_y, \quad \mathbf{v}_{12}^{(-1)r} = \mathbf{v}_{13}^{(-1)r} = \hat{\mathbf{e}}_x + i\hat{\mathbf{e}}_y, \quad \mathbf{v}_{12}^{(0)r} = \mathbf{v}_{13}^{(0)r} = \hat{\mathbf{e}}_z. \quad (\text{A1})$$

In contrast, only three nontrivial elements in $\mathbf{v}_{ls}^{(m)r}$ contribute to rotation:

$$\mathbf{v}_{11}^{(1)r} = -\hat{\mathbf{e}}_x - i\hat{\mathbf{e}}_y, \quad \mathbf{v}_{11}^{(-1)r} = \frac{1}{2}\hat{\mathbf{e}}_x - \frac{i}{2}\hat{\mathbf{e}}_y, \quad \mathbf{v}_{11}^{(0)r} = \hat{\mathbf{e}}_z. \quad (\text{A2})$$

Equations (A1) and (A2) give us all possible boundary conditions related to the motion of a rigid sphere.

Second, we derive $\mathbf{w}_{\lambda'\sigma'}^{(m)Q+}$ representing force or torque generated by a regular basis function. Net force can be derived by the surface integral of stress at the spherical interface. Then we apply the divergence theorem to simplify our calculation, whose details are as below:

$$\mathbf{w}_{\lambda'\sigma'}^{(m)t+} = \int_{p.s.} \hat{n} \cdot \bar{\bar{\sigma}}_{\lambda'm\sigma'} dA = \int_{p.v.} \nabla \cdot \bar{\bar{\sigma}}_{\lambda'm\sigma'} dV = i\Omega \int_{p.v.} \mathbf{v}_{\lambda'm\sigma'}^+ dV, \quad (\text{A3})$$

where $\bar{\bar{\sigma}}_{\lambda'm\sigma'}$ represents the fluid stress tensor, and \hat{n} means the normal unit vector pointing outward on the particle surface. The area integral on the particle surface is denoted by $\int_{p.s.} \cdots dA$, whereas $\int_{f.v.} \cdots dV$ is volume integral inside the solid volume. Like $\mathbf{v}_{ls}^{(m)t}$, most of elements in $\mathbf{w}_{\lambda'\sigma'}^{(m)t+}$ representing force disappear—the only nonzero elements correspond to $\lambda'=1$, $\sigma'=2,3$ so that nontrivial components are given by

$$\begin{cases} \mathbf{w}_{12}^{(1)t+} = \frac{8}{3}\pi k^2(k \cosh k - \sinh k)\hat{\mathbf{e}}_x + \frac{8}{3}i\pi k^2(k \cosh k - \sinh k)\hat{\mathbf{e}}_y \\ \mathbf{w}_{12}^{(0)t+} = -\frac{8}{3}\pi k^2(k \cosh k - \sinh k)\hat{\mathbf{e}}_z \\ \mathbf{w}_{12}^{(-1)t+} = -\frac{4}{3}\pi k^2(k \cosh k - \sinh k)\hat{\mathbf{e}}_x + \frac{4}{3}i\pi k^2(k \cosh k - \sinh k)\hat{\mathbf{e}}_y \end{cases} \quad (\text{A4})$$

and

$$\begin{cases} \mathbf{w}_{13}^{(1)t+} = \frac{4}{3}\pi\hat{\mathbf{e}}_x + \frac{4}{3}i\pi\hat{\mathbf{e}}_y \\ \mathbf{w}_{13}^{(0)t+} = -\frac{4}{3}\pi\hat{\mathbf{e}}_z \\ \mathbf{w}_{13}^{(-1)t+} = -\frac{2}{3}\pi\hat{\mathbf{e}}_x + \frac{2}{3}i\pi\hat{\mathbf{e}}_y. \end{cases} \quad (\text{A5})$$

Similarly, the torque associated with the regular basis function is obtained by

$$\begin{aligned} \mathbf{w}_{\lambda'\sigma'}^{(m)r+} &= - \int_{p.s.} (\hat{n} \cdot \bar{\bar{\sigma}}_{\lambda'm\sigma'}) \times \mathbf{r} dA = - \int_{p.v.} \nabla \cdot (\bar{\bar{\sigma}}_{\lambda'm\sigma'} \times \mathbf{r}) dV = - \int_{p.v.} (\nabla \cdot \bar{\bar{\sigma}}_{\lambda'm\sigma'}) \times \mathbf{r} dV \\ &+ \int_{p.v.} \bar{\bar{\sigma}}_{\lambda'm\sigma'} : \bar{\bar{\epsilon}} \cdot \bar{\bar{I}} = - \int_{p.v.} (\nabla \cdot \bar{\bar{\sigma}}_{\lambda'm\sigma'}) \times \mathbf{r} dV + 0 = -i\Omega \int_{p.v.} \mathbf{v}_{\lambda'm\sigma'}^+ \times \mathbf{r} dV. \end{aligned} \quad (\text{A6})$$

Here, $\bar{\bar{\epsilon}}$ represents a permutation tensor and $\bar{\bar{I}}$ denotes an identity tensor. The nonzero elements of torque in $\mathbf{w}_{\lambda'\sigma'}^{(m)r+}$ exist only for $\lambda'=1$, $\sigma'=1$:

$$\begin{cases} \mathbf{w}_{11}^{(1)r+} = \frac{8}{3}\pi[-3k \cosh k + (3+k^2) \sinh k]\hat{\mathbf{e}}_x - \frac{8}{3}i\pi[3k \cosh k - (3+k^2) \sinh k]\hat{\mathbf{e}}_y \\ \mathbf{w}_{11}^{(0)r+} = -\frac{8}{3}\pi[-3k \cosh k + (3+k^2) \sinh k]\hat{\mathbf{e}}_z \\ \mathbf{w}_{11}^{(-1)r+} = \frac{4}{3}\pi[3k \cosh k - (3+k^2) \sinh k]\hat{\mathbf{e}}_x - \frac{4}{3}i\pi[3k \cosh k - (3+k^2) \sinh k]\hat{\mathbf{e}}_y. \end{cases} \quad (\text{A7})$$

For Stokesian dynamics, the contributions in Eqs. (A4), (A5), and (A7) are identically zero—these appear here solely due to transient fluid inertia.

Third and finally, $\mathbf{w}_{\lambda\sigma}^{(m)Q-}$ means the force or torque associated with the singular basis function. The divergence theorem cannot be applied directly for analytical extension of the fields inside the solid volume due to the singularity at the center of the sphere. So we prefer to derive the opposite force exerted on the fluid instead of integrating inside the particle. Details are shown in the subsequent equation:

$$\begin{aligned} \mathbf{w}_{\lambda\sigma}^{(m)t-} &= \int_{p.s.} \hat{n} \cdot \bar{\bar{\sigma}}_{\lambda'm\sigma'} dA = - \left(\int_{f.s.} \hat{n} \cdot \bar{\bar{\sigma}}_{\lambda'm\sigma'} dA - \int_{\infty} \hat{n} \cdot \bar{\bar{\sigma}}_{\lambda'm\sigma'} dA \right) \\ &= -i\Omega \int_{f.v.} \nabla \cdot \bar{\bar{\sigma}}_{\lambda'm\sigma'} dV + \int_{\infty} \hat{n} \cdot \bar{\bar{\sigma}}_{\lambda'm\sigma'} dA = -i\Omega \int_{f.v.} \mathbf{v}_{\lambda m\sigma}^- dV + \int_{\infty} \hat{n} \cdot \bar{\bar{\sigma}}_{\lambda'm\sigma'} dA, \end{aligned} \quad (\text{A8})$$

where $\int_{\infty} \dots dA$ is the area integral at infinity, $\int_{f.s.} \dots dA$ is the area integral for the liquid domain including infinity as well as solid-fluid interface, and $\int_{f.v.} \dots dV$ is the volume integral of the entire fluid volume. All nontrivial elements in force $\mathbf{w}_{\lambda\sigma}^{(m)r-}$ are listed by

$$\begin{cases} \mathbf{w}_{12}^{(1)r-} = -\frac{8}{3}\pi e^{-k}(1+k)k^2\hat{\mathbf{e}}_x - \frac{8}{3}i\pi e^{-k}(1+k)k^2\hat{\mathbf{e}}_y \\ \mathbf{w}_{12}^{(0)r-} = \frac{8}{3}\pi e^{-k}(1+k)k^2\hat{\mathbf{e}}_z \\ \mathbf{w}_{12}^{(-1)r-} = \frac{4}{3}\pi e^{-k}(1+k)k^2\hat{\mathbf{e}}_x - \frac{4}{3}i\pi e^{-k}(1+k)k^2\hat{\mathbf{e}}_y \end{cases} \quad (\text{A9})$$

and

$$\begin{cases} \mathbf{w}_{13}^{(1)r-} = \frac{4}{3}\pi\hat{\mathbf{e}}_x + \frac{4}{3}i\pi\hat{\mathbf{e}}_y \\ \mathbf{w}_{13}^{(0)r-} = -\frac{4}{3}\pi\hat{\mathbf{e}}_z \\ \mathbf{w}_{13}^{(-1)r-} = -\frac{2}{3}\pi\hat{\mathbf{e}}_x + \frac{2}{3}i\pi\hat{\mathbf{e}}_y. \end{cases} \quad (\text{A10})$$

On the other hand, torque generated by the singular basis function is obtained by the same logic as that in Eqs. (A6) and (A8). Consequently, we find

$$\mathbf{w}_{\lambda\sigma}^{(m)r-} = -\int_{p.s.} (\hat{\mathbf{n}} \cdot \bar{\bar{\sigma}}_{\lambda'm\sigma'}) \times \mathbf{r} dA = i\Omega \int_{f.v.} \mathbf{v}_{lm\sigma}^- \times \mathbf{r} dV - \int_{\infty} (\hat{\mathbf{n}} \cdot \bar{\bar{\sigma}}_{\lambda'm\sigma'}) \times \mathbf{r} dA. \quad (\text{A11})$$

Finally, nonzero elements in torque $\mathbf{w}_{\lambda\sigma}^{(m)r-}$ are constructed as

$$\begin{cases} \mathbf{w}_{11}^{(1)r-} = \frac{8}{3}\pi e^{-k}(3+3k+k^2)\hat{\mathbf{e}}_x + \frac{8}{3}i\pi e^{-k}(3+3k+k^2)\hat{\mathbf{e}}_y \\ \mathbf{w}_{11}^{(0)r-} = -\frac{8}{3}\pi e^{-k}(3+3k+k^2)\hat{\mathbf{e}}_z \\ \mathbf{w}_{11}^{(-1)r-} = -\frac{4}{3}\pi e^{-k}(3+3k+k^2)\hat{\mathbf{e}}_x + \frac{4}{3}i\pi e^{-k}(3+3k+k^2)\hat{\mathbf{e}}_y. \end{cases} \quad (\text{A12})$$

After all of these elements are known, the friction tensors can be constructed using Eq. (27).

-
- [1] E. J. Stancik, A. L. Hawkinson, J. Vermant, and G. G. Fuller, Dynamic transitions and oscillatory melting of a two-dimensional crystal subjected to shear flow, *J. Rheol.* **48**, 159 (2004).
 - [2] F. F. Dizaji, J. S. Marshall, and J. R. Grant, Collision and breakup of fractal particle agglomerates in a shear flow, *J. Fluid Mech.* **862**, 592 (2019).
 - [3] J. Bławdziewicz and S. Bhattacharya, Comment on Drift without flux: Brownian walker with a space-dependent diffusion coefficient, *Europhys. Lett.* **63**, 789 (2003).
 - [4] J. F. Brady and J. F. Morris, Microstructure of strongly sheared suspensions and its impact on rheology and diffusion, *J. Fluid Mech.* **348**, 103 (1997).
 - [5] S. Bhattacharya, D. K. Gurung, and S. Navardi, Radial distribution and axial dispersion of suspended particles inside a narrow cylinder due to mildly inertial flow, *Phys. Fluids* **25**, 033304 (2013).
 - [6] V. Seshadri and S. P. Sutera, Concentration changes of suspensions of rigid spheres flowing through tubes, *J. Colloid Interface Sci.* **27**, 101 (1968).
 - [7] S. Bhattacharya, D. K. Gurung, and S. Navardi, Radial lift on a suspended finite-sized sphere due to fluid inertia for low-Reynolds-number flow through a cylinder, *J. Fluid Mech.* **722**, 159 (2013).
 - [8] Marcos, H. C. Fu, T. R. Powers, and R. Stocker, Separation of Microscale Chiral Objects by Shear Flow, *Phys. Rev. Lett.* **102**, 158103 (2009).
 - [9] M. Frank, D. Anderson, E. R. Weeks, and J. F. Morris, Particle migration in pressure-driven flow of a Brownian suspension, *J. Fluid Mech.* **493**, 363 (2003).
 - [10] Z. Li and G. Drazer, Separation of Suspended Particles by Arrays of Obstacles in Microfluidic Devices, *Phys. Rev. Lett.* **98**, 050602 (2007).

- [11] S. Navardi, S. Bhattacharya, and H. Wu, Stokesian simulation of two unequal spheres in a pressure-driven flow through a cylinder, *Comput. Fluids* **121**, 145 (2015).
- [12] T. G. Mason, K. Ganesan, J. H. van Zanten, D. Wirtz, and S. C. Kuo, Particle Tracking Microrheology of Complex Fluids, *Phys. Rev. Lett.* **79**, 3282 (1997).
- [13] T. M. Squires, Nonlinear microrheology: Bulk stresses versus direct interactions, *Langmuir* **24**, 1147 (2008).
- [14] J. A. Eastman, S. U. S. Choi, S. Li, W. Yu, and L. J. Thompson, Anomalous increased effective thermal conductivities of ethylene glycol-based nanofluids containing copper nanoparticles, *Appl. Phys. Lett.* **78**, 718 (2001).
- [15] J. M. Kincaid and E. G. D. Cohen, Nano- and pico-scale transport phenomena in fluids, *J. Stat. Phys.* **109**, 361 (2002).
- [16] R. B. Jones, Spherical particle in Poiseuille flow between planar walls, *J. Chem. Phys.* **121**, 483 (2004).
- [17] B. Cichocki and R. B. Jones, Image representation of a spherical particle near a hard wall, *Physica A* **258**, 273 (1998).
- [18] L. J. Durlofsky and J. F. Brady, Dynamic simulation of bounded suspensions of hydrodynamically interacting particles, *J. Fluid Mech.* **200**, 39 (1989).
- [19] S. Navardi and S. Bhattacharya, General methodology to evaluate two-particle hydrodynamic friction inside cylinder-bound viscous fluid, *Comput. Fluids* **76**, 149 (2013).
- [20] T. N. Phung, J. F. Brady, and G. Bossis, Stokesian dynamics simulation of Brownian suspensions, *J. Fluid Mech.* **313**, 181 (1996).
- [21] A. S. Sangani and G. Mo, An $O(N)$ algorithm for Stokes and Laplace interactions of particles, *Phys. Fluids* **8**, 1990 (1996).
- [22] A. Sierou and J. F. Brady, Accelerated Stokesian dynamics simulations, *J. Fluid Mech.* **448**, 115 (2001).
- [23] B. U. Felderhof, Estimating the viscoelastic moduli of a complex fluid from observation of Brownian motion, *J. Chem. Phys.* **131**, 164904 (2009).
- [24] B. U. Felderhof, Estimating the viscoelastic moduli of complex fluids from observation of Brownian motion of a particle confined to a harmonic trap, *J. Chem. Phys.* **134**, 204910 (2011).
- [25] A. M. Leshansky, O. M. Lavrenteva, and A. Nir, The leading effect of fluid inertia on the motion of rigid bodies at low Reynolds number, *J. Fluid Mech.* **505**, 235 (2004).
- [26] H. Clercx and P. Schramm, Brownian particles in shear flow and harmonic potential, *Phys. Rev. A* **46**, 1942 (1992).
- [27] H. Clercx and P. Schramm, Retarded hydrodynamic interactions in suspensions, *Physica A* **174**, 325 (1991).
- [28] B. U. Felderhof, Retarded hydrodynamic interaction between two spheres immersed in a viscous incompressible fluid, *Phys. Fluids* **31**, 053604 (2019).
- [29] B. Liu and S. Bhattacharya, Vector field solution for Brinkman equation in presence of disconnected spheres, *Phys. Rev. Fluids* **5**, 104303 (2020).
- [30] B. Cichocki, B. U. Felderhof, and R. Schmitz, Hydrodynamic interactions between two spherical particles, PCH, *PhysicoChem. Hydrodyn.* **10**, 383 (1988).
- [31] R. G. Cox and H. Brenner, The slow motion of a sphere through a viscous fluid towards a plane surface-II Small gap widths, including inertial effects, *Chem. Eng. Sci.* **22**, 1753 (1967).